IEEJ Journal of Industry Applications
Vol.6 No.6 pp.401–408 DOI: 10.1541/ieejjia.6.401

Paper

Influence of Permanent Magnet Properties and Arrangement on Performance of IPMSMs for Automotive Applications

Yuki Shimizu* Student Member, Shigeo Morimoto*a) Senior Member
Masayuki Sanada* Senior Member, Yukinori Inoue* Member

(Manuscript received Jan. 16, 2017, revised May 26, 2017)

Nowadays, interior permanent magnet synchronous motors (IPMSMs) are widely utilized as traction motors. The permanent magnets used in IPMSMs are an important factor; thus, high-coercivity permanent magnets with lesser rare-earth elements are in development. This study investigated the performance of IPMSMs typically used in automotive applications modified to contain a strong magnet model (SMM). Rotor models with two permanent magnet arrangements, that is, a V-shaped single-layered permanent magnet structure (Type 1V) and a double-layered permanent magnet structure (Type 2D), were considered in this study. This paper discusses the characteristics of the analysis models based on the results of a two-dimensional finite element analysis. The maximum torques of Types 1V and 2D with the SMMs were approximately the same. In addition, the loss of Type 2D with the SMM was lower than that of Type 1V with the SMM at two evaluation points and under two driving schedules. Therefore, Type 2D was proved to be suitable for use with the SMM.

Keywords: interior permanent magnet synchronous motor (IPMSM), traction motor, strong magnet, magnet arrangement, emission test cycle

1. Introduction

In response to the environmental pollution caused by vehicles and the increasing emissions of greenhouse gases, such as carbon dioxide, the development of hybrid vehicles (HVs), electric vehicles (EVs) and fuel cell vehicles (FCVs), which are electrically driven by traction motors, has become increasingly important [1]. The traffic environment and driving modes of these eco-friendly cars require a wide range of operation conditions. Accordingly, the necessary characteristics of traction motors of such cars are as follows [2]:

1) high torque density and power density,
2) wide operation area,
3) high efficiency over wide torque and speed ranges,
4) high reliability and robustness,
5) small and light-weight form,
6) low acoustic noise, and
7) reasonable cost.

To develop a motor with these characteristics, interior permanent magnet synchronous motors (IPMSMs) are commonly utilized as vehicle drive motors [3]–[6]. IPMSMs generate a high total torque by combining the magnet torque caused by permanent magnets (PMs) and the reluctance torque caused by the magnetic saliency. Moreover, flux weakening (FW) control ensures that the motor terminal voltage does not exceed the maximum voltage output of the inverter at high speeds, allowing the motor to maintain a high torque density and high efficiency over wide ranges of torque and speed.

The magnetic materials used in IPMSMs are an important factor in determining their performance, which is particularly strongly influenced by the PMs they contain [7]. However, the PMs used in conventional traction motors have the disadvantage of increasing price and providing an unstable supply of rare-earth materials, such as neodymium and dysprosium. This problem has led to an investigation of high-coercivity PMs with lesser rare-earth elements, especially lesser heavy ones [8].

IPMSMs with higher-remanence PMs are expected to provide a higher torque derived from increasing magnetic flux linkage and magnet torque [7]. However, there is the risk that the torque may not be as high as expected because of magnetic saturation; moreover, iron loss increases with increasing magnetic flux density. For this reason, the optimal rotor structure of IPMSMs with higher-remanence PMs should be examined.

Hence, this paper investigates the performance of two modified versions of IPMSMs typically used in automotive applications and compares them with a reference model. The modified IPMSMs use a strong magnet model (SMM) designed to have the properties of $NdFe_{12}N_x$, which is a novel hard-magnetic compound developed by Hirayama et al. [8]. The IPMSM rotor models have two PM arrangements, a V-shaped single-layered PM structure and a double-layered PM structure. This paper discusses the characteristics of the analysis models based on the results of two-dimensional (2-D) finite element analysis by JMAG-Designer 14.1.

2. Analysis Models

The reference model in this paper is defined as an IPMSM

a) Correspondence to: Shigeo Morimoto. E-mail: morimoto@eis.osakafu-u.ac.jp
* Osaka Prefecture University
1-1, Gakuencho, Naka-ku, Sakai, Osaka 599-8531, Japan

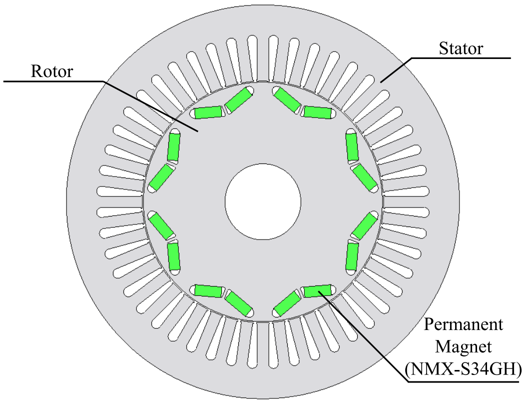

Fig. 1. Cross section of the reference model (Type 1V_R)

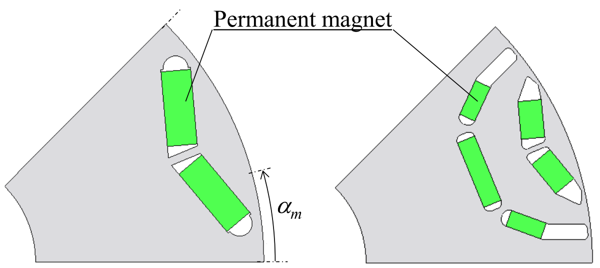

(a) Type 1V. (b) Type 2D.

Fig. 2. Rotor structure (single pole)

Table 1. Motor specifications

Item (Unit)		Type 1V_R	Type 2D_R	Type 1V_N	Type 2D_N
Number of pole/slot		8/48			
Stator diameter (mm)		264			
Rotor diameter (mm)		160.4			
Air gap length (mm)		0.75			
Shaft diameter (mm)		51			
Stack length (mm)		50			
Winding resistance*1 (Ω)		0.129			
Rotor structure		1V	2D	1V	2D
Iron core	B_{10}*2 (T)	1.50			
	B_{30}*2 (T)	1.61			
	B_{50}*2 (T)	1.69			
	B_{100}*2 (T)	1.81			
	$W_{10/50}$*3 (W/kg)	0.918			
PM material		NMX-S34GH		Strong Magnet (NdFe12N)	
	Remanence*1 (T)	0.99		1.35	
	Coercivity*4 (kA/m)	752		1023	
	Volume (cm^3)	100			

*1 Under the condition that the temperature is 180 °C.
*2 Flux density B_x when the magnetic field is $x \times 10^2$ A/m.
*3 Iron loss when the frequency is 50 Hz and the maximum flux density is 1.0 T.
*4 Out of consideration of the demagnetization influence.

with a V-shaped single-layered PM structure, which is designed based on the third-generation Prius traction motor [9]. Figure 1 shows a cross section of the reference model (Type 1V_R). The stator has eight poles and a distributed winding with 48 slots.

Figure 2 shows the rotor structures of the analysis models, Table 1 lists their motor specifications, and Fig. 3 shows the demagnetization curves of two types of permanent magnets. The Type 1V model has a V-shaped single-layered PM structure, and the Type 2D model has a double-layered PM structure intended to increase the reluctance torque in comparison with the Type 1V model, as the authors previously proposed

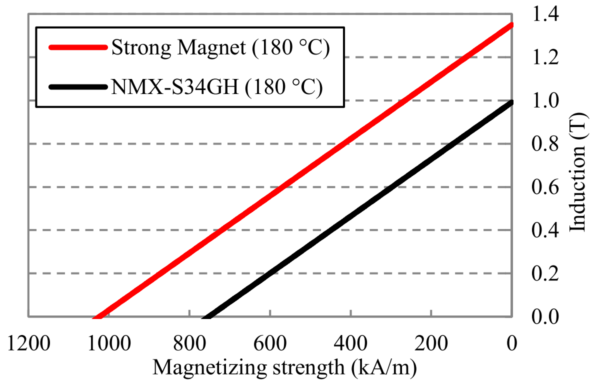

Fig. 3. Demagnetization curve

in reference (10). Additionally, Types 1V_R and 2D_R are Types 1V and 2D models using the conventional magnet NMX-S34GH, respectively, and Types 1V_N and 2D_N are Types 1V and 2D models using the SMM, respectively.

The SMM is assumed to have a higher remanence calculated from 95% volume fraction and texture of the main phase respectively with high magnetization shown in reference (8). The coercivity of the SMM is assumed to be 25% of the anisotropic magnetic field.

3. Analytical Results

3.1 No-Load Air-Gap Flux Density Figure 4 compares the no-load air-gap flux densities of the analysis models, where the mechanical angle α_m is defined as shown in Fig. 2(a) and the total harmonic distortion (THD) is calculated as

$$\mathrm{THD} = \frac{\sqrt{\sum_{i=2}^{\infty} B_{gi}^2}}{B_{g1}} \times 100 \quad (\%), \cdots\cdots\cdots\cdots\cdots\cdots (1)$$

where B_{gi} is the i th order harmonic component of the air-gap flux density.

Comparing models with the same structure and different PMs, the fundamental components of the no-load air-gap flux densities of Types 1V_N and 2D_N are higher than those of Types 1V_R and 2D_R. Additionally, comparing models with the same PM and different structures, the fundamental components of the no-load air-gap flux densities of the Type 2D models are smaller than those of the Type 1V models. This is because that the PM arrangement of Type 1V is more central and closer to the air gap. Furthermore, the angular distribution of the flux density of Type 2D extends to a wider range and resembles a sinusoidal wave. The reason of this is that the PMs of the Type 2D models exert an influence throughout a wider range of the air gap as a result of the double-layered PM structure and the sufficient quantity of PMs in the second layer. Consequently, the harmonic components of the flux densities of the Type 2D models relative to their fundamental component are lower than those of the Type 1V models, resulting in these models having the lower THD.

3.2 Motor Parameters Figure 5 compares plots of the inductance against the current phase angle for the different models, where the phase current I_e was set to 134 A (the current density J_e = 17.6 A/mm^2). L_d and L_q are the d- and q-axis inductance, respectively, and the current phase angle

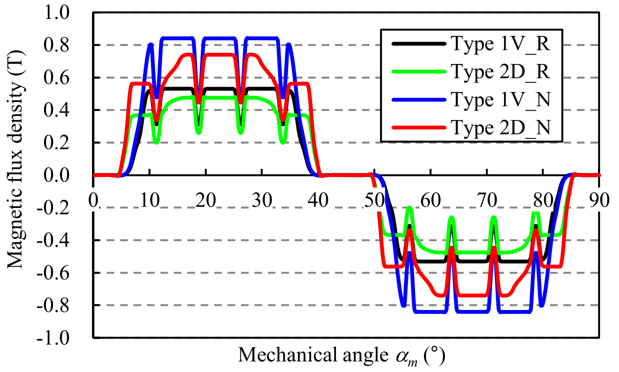

(a) Angular distribution.

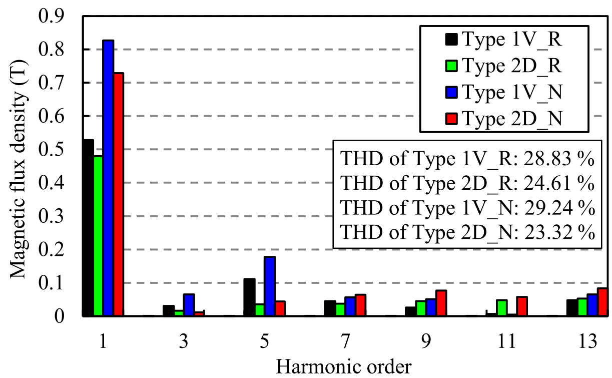

(b) Harmonic components.

Fig. 4. Air-gap flux density (no load)

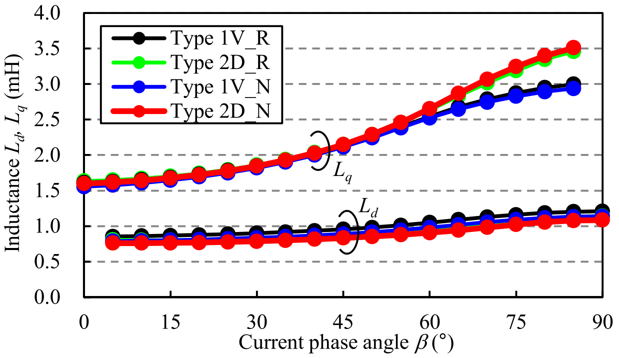

Fig. 5. Inductance plotted against current phase angle (I_e = 134 A)

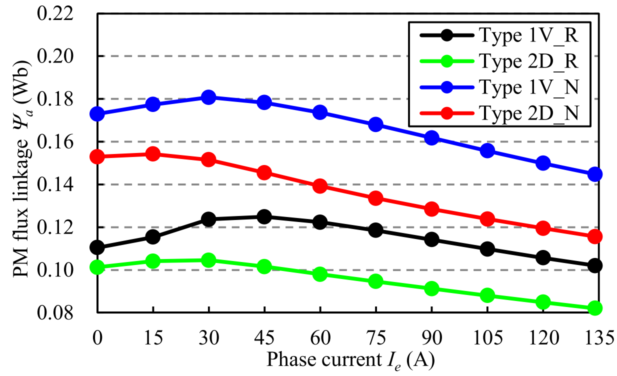

Fig. 6. PM flux linkage plotted against phase current characteristics

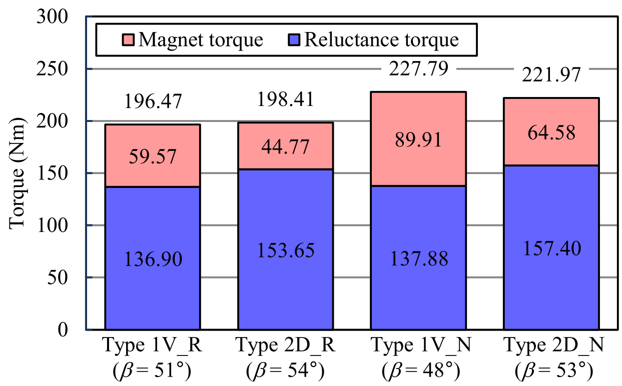

Fig. 7. Maximum torque characteristics (I_e = 134 A)

Table 2. Motor parameters (I_e = 134 A)

Item (Unit)	Type 1V_R	Type 2D_R	Type 1V_N	Type 2D_N
L_d (mH)	0.99	0.92	0.90	0.87
L_q (mH)	2.28	2.42	2.19	2.39
L_q - L_d (mH)	1.30	1.50	1.29	1.52
Ψ_a (Wb)	0.102	0.082	0.145	0.116
Ψ_{dmin}* (Wb)	-0.178	-0.183	-0.119	-0.136

* Calculated from the results under β = 90°.

β is the leading angle of the current vector from the q-axis. The inductances L_d of the Type 2D models are lower than those of the Type 1V models. The reason for this is that the d-axis magnetic reluctance of the magnetic path in Type 2D is larger because of its double-layered PM structure. In contrast, the inductances L_q of the Type 2D models are higher than those of the Type 1V models in the region of large β. This is because the Type 2D models have the wide q-axis magnetic path, yielding higher L_q in the region of large β, where the influence of the magnetic saturation is mitigated. These results reveal that the properties of the magnet do not affect the inductance characteristics.

Figure 6 compares plots of the PM flux linkage against the phase current, where the PM flux linkage Ψ_a was calculated for β = 0°. The flux linkage Ψ_a of Type 1V_N is the highest among the models, followed by those of Types 2D_N, 1V_R and 2D_R, as a result of the fundamental component of the no-load air-gap flux density shown in Fig. 4. In addition, the plots of the PM flux linkage against the phase current for the Type 2D models are different from those for the Type 1V models and decrease almost monotonically. This is because the narrower outer rib of Type 2D causes magnetic saturation even in the region of small I_e.

3.3 Maximum Torque and Power Characteristics

Figure 7 shows the torque characteristics of each model under the maximum torque per ampere (MTPA) control, Table 2 compares the typical motor parameters of the analysis models, and Fig. 8 shows the flux density distributions. In all of Fig. 7, Table 2 and Fig. 8, I_e = 134 A.

Comparing models with the same structure and different PMs, the maximum total torques of Types 1V_N and 2D_N are larger than those of Types 1V_R and 2D_R by approximately 16% and 12%, respectively. This is because the flux linkages Ψ_a of Types 1V_N and 2D_N are larger, and the magnet torques increase. Similarly, comparing models with the same PM and different rotor structures, the maximum total torques of Types 1V_R and 2D_R are approximately the same, and those of Types 1V_N and 2D_N are also approximately the same. The reason for this is that the magnet

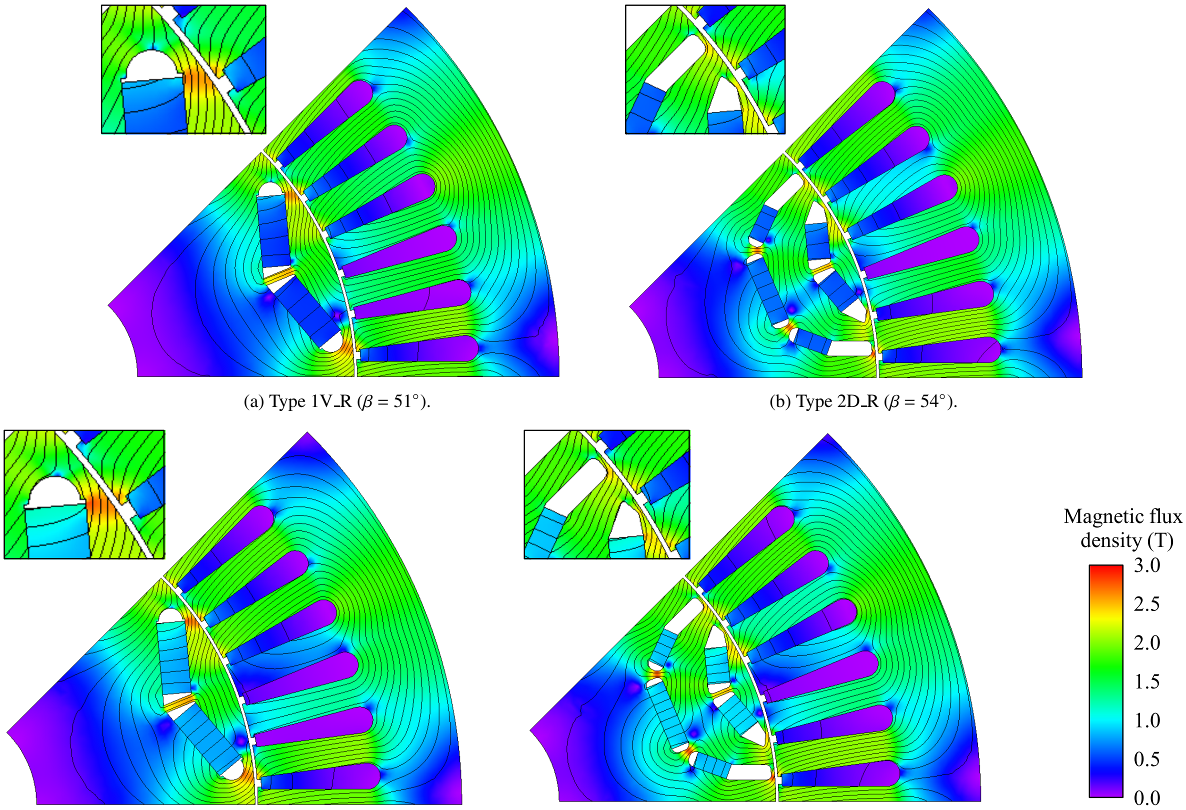

(a) Type 1V_R ($\beta = 51°$). (b) Type 2D_R ($\beta = 54°$). (c) Type 1V_N ($\beta = 48°$). (d) Type 2D_N ($\beta = 53°$).

Fig. 8. Flux density distributions and magnetic flux lines under MTPA control (I_e = 134 A)

torques of the Type 2D models are smaller than those of the Type 1V models because of the smaller flux linkages Ψ_a of the Type 2D models, and the reluctance torques of the Type 2D models are larger because of the higher inductance differences L_q–L_d of the Type 2D models.

The parameter $\Psi_{d\min}$ in Table 2 is the minimum d-axis flux linkage and is defined as

$$\Psi_{d\min} = \Psi_a - L_d I_{am} = \Psi_a - \sqrt{3} L_d I_{em}, \cdots\cdots\cdots\cdots (2)$$

where I_{am} is the maximum armature current and I_{em} is the maximum phase current. $\Psi_{d\min}$ is an important parameter in estimating the constant power speed range (CPSR). If $\Psi_{d\min} > 0$, the motor cannot drive above a certain speed under FW control. Conversely, if $\Psi_{d\min} < 0$, the conversion to maximum torque per voltage (MTPV) control at high speeds allows the motor to reach infinite speed; in addition, as $\Psi_{d\min}$ decreases, the maximum power decreases and the CPSR narrows. Furthermore, the $\Psi_{d\min}$ value at which the highest maximum power and the widest CPSR can be obtained is $\Psi_{d\min}$ = 0, i.e., $\Psi_a = L_d I_{am}$. As shown in Table 2, $\Psi_{d\min}$ is negative for every model, and that of Type 1V_N is the highest among the models, followed by Types 2D_N, 1V_R and 2D_R. This is attributable to the flux linkage Ψ_a of Type 1V_N being the highest among the models and the inductance L_d being approximately the same for every model. Hence, the operation area of Type 2D_N is estimated to be the widest.

Figure 9 compares plots of the power against the speed for each model, where I_{em} = 134 A and the maximum terminal voltage V_{am} = 507 V because the DC link voltage V_{DC} is assumed to be 650 V.

In the speed region below the base speed (under MTPA control), the power of each model is proportional to the maximum torque shown in Fig. 7. In addition, in the speed region above the base speed (under FW and MTPV control), the plots of the power against the speed of Type 1V_N are the highest among the models, followed by those of Types 2D_N, 1V_R and 2D_R; this order is the same for the order of $\Psi_{d\min}$.

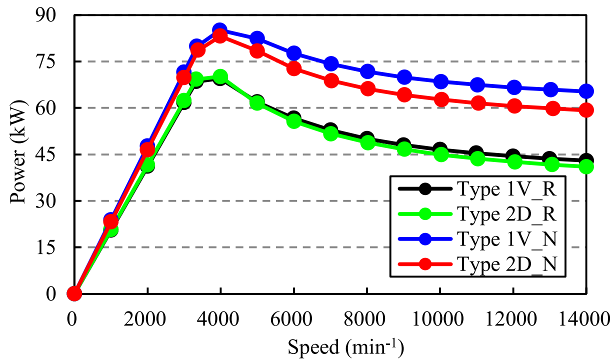

Fig. 9. Power plotted against speed (I_{em} = 134 A, V_{am} = 507 V)

As a result, the maximum torques of Types 1V_N and 2D_N are approximately equal and larger than that of the reference model Type 1V_R. In addition, the power plotted against the speed for Type 1V_N is higher than that for Type 2D_N, yet the operation area of Type 2D_N is wider than that of the reference model Type 1V_R.

3.4 Loss Characteristics at Evaluation Points

Considering the operation of an actual EV, conditions for city driving (20 Nm, 3500 min^{-1}) and highway driving (20 Nm, 11000 min^{-1}) were defined as evaluation points. The

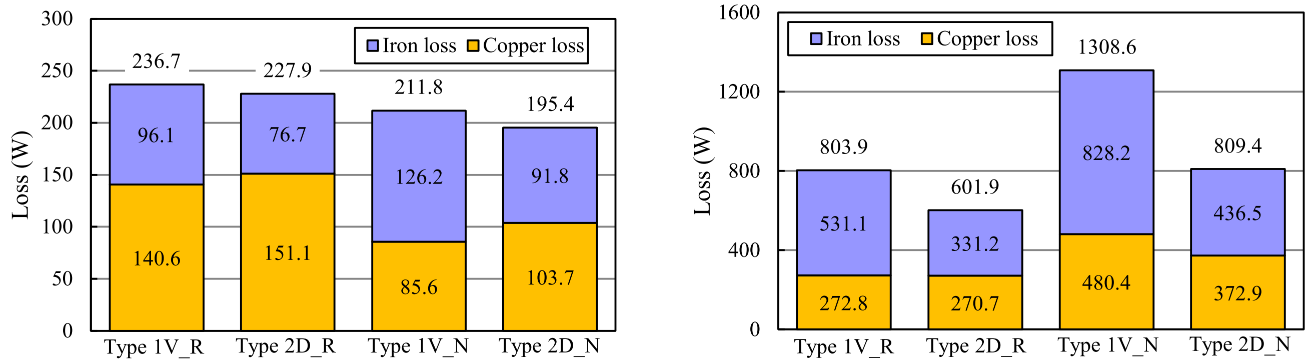

(a) City driving evaluation point (20 Nm, 3500 min^{-1}). (b) Highway driving evaluation point (20 Nm, 11000 min^{-1}).

Fig. 10. Loss characteristics at the evaluation points under maximum efficiency control

Table 3. Properties with maximum efficiency at different evaluation points

(a) City driving evaluation point (20 Nm, 3500 min^{-1}).

Item (Unit)	Type 1V_R	Type 2D_R	Type 1V_N	Type 2D_N
I_e (A)	19.1	19.8	14.9	16.4
β (°)	34.1	39.0	27.7	34.6
V_a (V)	246.9	239.3	289.7	264.6
η (%)	96.83	96.95	97.14	97.37

(b) Highway driving evaluation point (20 Nm, 11000 min^{-1}).

Item (Unit)	Type 1V_R	Type 2D_R	Type 1V_N	Type 2D_N
I_e (A)	26.6	26.5	35.3	31.1
β (°)	64.8	65.4	76.8	74.2
V_a (V)	506.3	505.6	506.4	506.1
η (%)	96.55	97.40	94.47	96.55

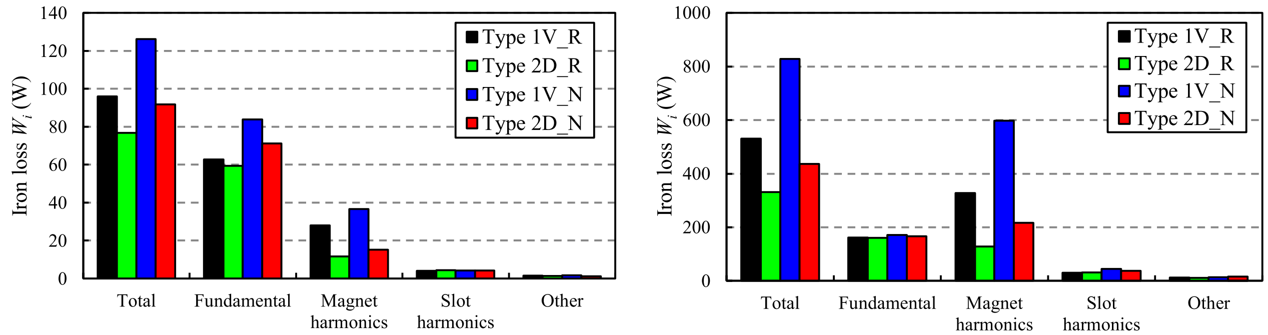

(a) City driving evaluation point (20 Nm, 3500 min^{-1}). (b) Highway driving evaluation point (20 Nm, 11000 min^{-1}).

Fig. 11. Iron losses categorized according to the origins of the loss at the evaluation points

loss characteristics of the analysis models were compared at these evaluation points under maximum efficiency control. Figure 10 and Table 3 show the loss characteristics and the other properties at the evaluation points, respectively, where I_{em} = 134 A and V_{am} = 507 V. V_a is the terminal voltage, and η is the efficiency.

Comparing the loss characteristics at the city driving evaluation point, the loss of Type 2D_N is the lowest, followed by those of Types 1V_N, 2D_R and 1V_R. This is because the models with the SMM require a smaller current than the models with NMX-S34GH to achieve the same torque, resulting in a reduction in the copper loss; furthermore, the Type 2D models produce the smaller iron loss than those of the Type 1V models. Comparing the loss characteristics at the highway driving evaluation point, the loss of Type 1V_N is the highest and that of Type 2D_R is the lowest among the models, and the losses of Types 1V_R and 2D_N are approximately equal. This is because FW control for the models with the SMM requires a higher current, leading to higher copper loss. Additionally, the iron loss is also higher in Type 1V_N than in Type 1V_R because the SMM has a higher remanence than the conventional magnet. However, Type 2D_N achieved smaller iron loss because of the smallest THD, resulting in a higher efficiency.

To understand the cause of the differences in the iron losses of each model, the calculated iron losses were categorized according to the origin of the loss at the two evaluation points. Figure 11 shows the results of this categorization. The magnet harmonics are the sum of the odd-order harmonic components, excluding the fundamental component, and the slot harmonics are the sum of the multiples of 12th-order harmonic components that occurred with the motor rotation [11]. For each evaluation point, the iron loss originating from the magnet harmonics of the Type 2D models are lower than those of the Type 1V models. This is attributable to the Type 2D models having the lower THD, as shown in Fig. 4.

3.5 Efficiency Characteristics Comprehensively judging from the output characteristics shown in Fig. 9 and the loss characteristics shown in Fig. 10, it can be concluded that Type 2D_N has the highest performance among the analysis models, and the Type 2D model is suitable for use with the SMM. In the following section, therefore, the efficiency characteristic of Type 2D_N is compared with the reference model. Figure 12 shows the efficiency maps of Types 1V_R and 2D_N, and Fig. 13 shows the efficiency difference maps for Type 2D_N with Type 1V_R. The operation area used to make this efficiency difference map was that of Type 1V_R.

The efficiency difference map indicates that the efficiency

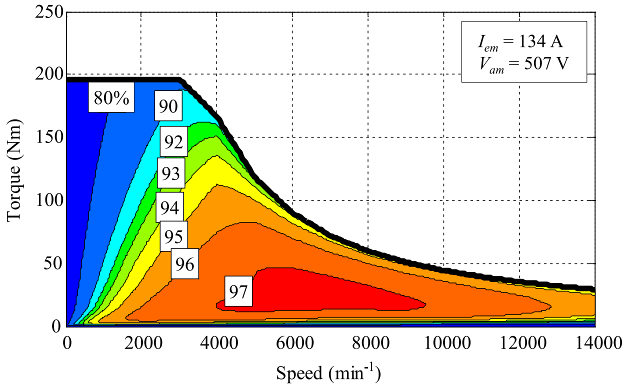

(a) Type1V_R.

(b) Type 2D_N.

Fig. 12. Efficiency maps (unit: %)

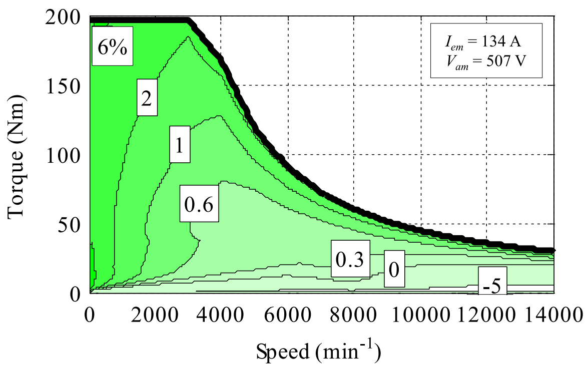

Fig. 13. Efficiency difference map of between Types 2D_N and 1V_R (unit: %)

of Type 2D_N is higher than that of Type 1V_R in almost the entire operation area. This is because a smaller current is used in Type 2D_N to generate the same torque in the low-speed region, resulting in a reduction in the copper loss, which is dominant at low speeds. In the high-speed low-torque region, FW control for Type 2D_N requires a higher current, leading to a higher copper loss, whereas the lower THD of Type 2D_N shown in Fig. 3 yields a lower iron loss, resulting in the higher efficiency.

3.6 Loss Characteristics under Driving Schedules

Two driving schedules, the urban dynamometer driving schedule (UDDS) and the highway fuel economy test (HWFET) cycles, which represent city and highway driving conditions similar to those in the United States, respectively, were selected to evaluate the loss characteristics.

Figure 14 shows the vehicle speed settings under these two

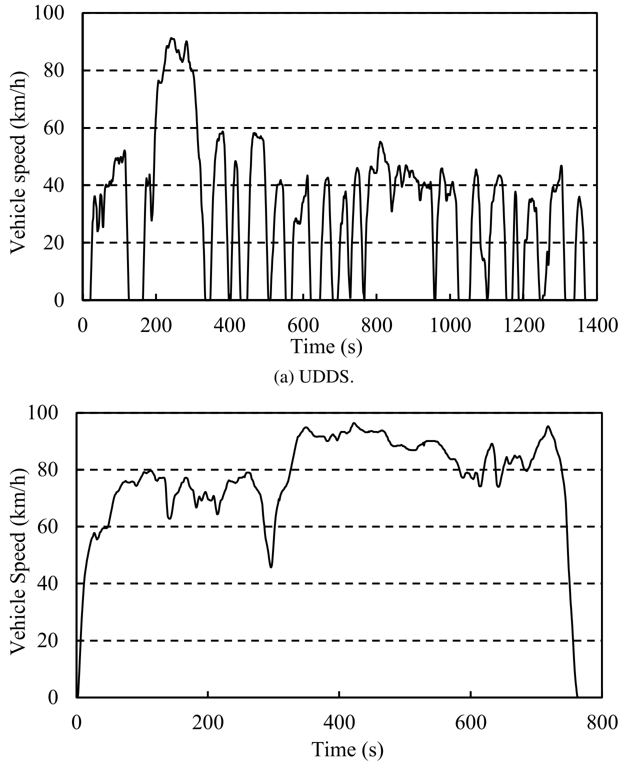

(a) UDDS.

(b) HWFET.

Fig. 14. Vehicle speed settings under different driving cycles

driving schedules. The running resistance R_0, which is used in calculation of the loss under these driving schedules, consists of the aerodynamic resistance R_a, the rolling resistance R_r, and the acceleration resistance R_c as follows:

$$R_0 = R_a + R_r + R_c, \quad (3)$$

$$R_a = \frac{1}{2}\rho C_d A V^2, \quad (4)$$

$$R_r = C_{rr} M g, \quad (5)$$

$$R_C = M_i a, \quad (6)$$

where ρ is the density of air, C_d is the aerodynamic drag coefficient, A is the projected frontal area, V is the vehicle velocity, C_{rr} is the rolling drag coefficient, M is the vehicle mass, g is the gravitational acceleration, M_i is the standard equivalent inertia weight, and a is the acceleration. Moreover, by using the motor torque T, the transmission output force F_t is calculated as

$$F_t = \eta_t \frac{\alpha T}{r}, \quad (7)$$

where η_t is the transmission efficiency, α is the reduction gear ratio, and r is the tire radius. Because of the balance between the running resistance R_0 and the transmission output force F_t, the motor torque T is calculated as

$$T = \frac{r}{\alpha \eta_t}(R_a + R_r + R_c). \quad (8)$$

Table 4 shows the constant values used in calculation of torques under driving schedules. By using (8) and the values in Table 4, discrete operating points every one second under two driving schedules were calculated and shown in Fig. 15.

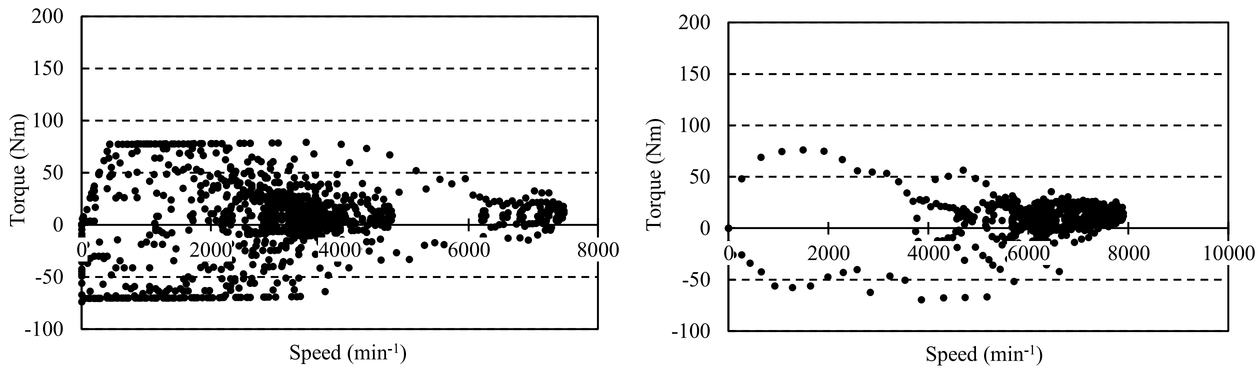

(a) UDDS. (b) HWFET.

Fig. 15. Discrete operating points under different driving cycles

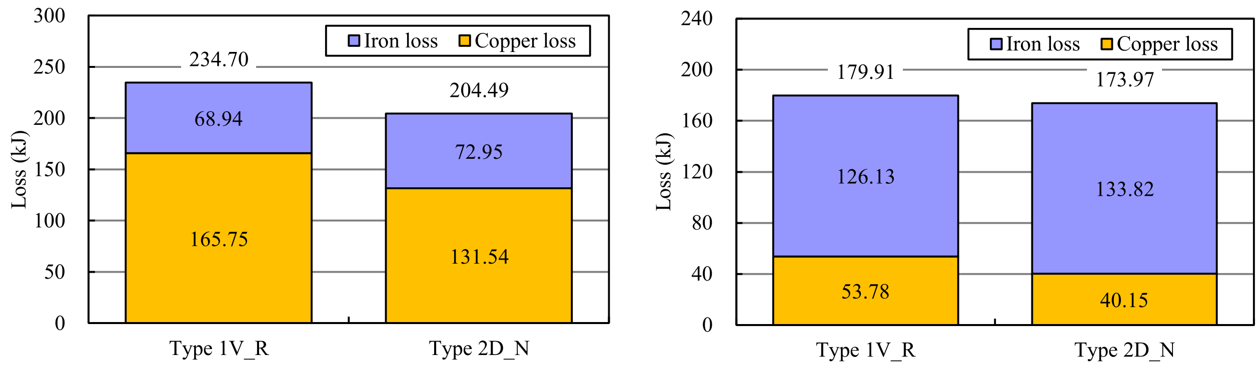

(a) UDDS. (b) HWFET.

Fig. 16. Loss characteristics under different driving cycles

Table 4. Constant values used in calculation of torques under driving schedules

Item (Unit)	Value
Density of air ρ (kg/m^3)	1.205 (1 atm, 20 °C)
Aerodynamic drag coefficient C_d	0.25
Projected frontal area A (m^2)	2.321
Rolling drag coefficient C_{rr}	0.007
Vehicle mass M (kg)	1460
Gravitational acceleration g (m/s^2)	1470
Standard equivalent inertia weight M_i (kg)	9.807
Transmission efficiency η_t (%)	95
Reduction gear ratio α	9.592
Tire radius r (mm)	621

Furthermore, the losses of analysis models at each point in Fig. 15 were calculated and summed up. Figure 16 shows the calculation result, where only positive torque was used to calculate the loss characteristics in order to ignore the regenerative brake.

Comparing the loss characteristics under the UDDS cycle, the loss of Type 2D_N is lower than that of Type 1V_R. This is because the UDDS operating points are concentrated at low and medium speeds, at which the efficiency of Type 2D_N is higher, as shown in Fig. 13. Comparing the loss characteristics under the HWFET cycle, the loss of Type 2D_N is also lower. This is because that HWFET operating points are concentrated at high speeds, at which the iron loss of Type 2D_N is lower because it has the lowest THD, as shown in Fig. 4, resulting in lower loss than the reference model Type 1V_R.

4. Conclusions

This paper investigated the performance of IPMSMs used in automotive applications that were modified to contain SMMs and compared them with a reference model. The IPMSM rotor models had two PM arrangements, a V-shaped single-layered PM structure and a double-layered PM structure. The characteristics of the analysis models were discussed based on the results of 2-D finite element analysis. The analysis and comparison results are summarized as follows.

The maximum torques produced by Types 1V_N and 2D_N were approximately the same and were larger than those of the models with the conventional magnets. In addition, the power plotted against the speed for Type 1V_N was higher than that of Type 2D_N, yet both operation areas of models with SMM were wider than that of the reference model Type 1V_R. Furthermore, the loss of Type 1V_N was higher than that of Type 2D_N at the two considered evaluation points. Additionally, the efficiency of Type 2D_N was higher than that of Type 1V_R in nearly the entire operation area, and the loss of Type 2D_N was lower than that of Type 1V_R under the two considered driving cycles.

Hence, despite its smaller operation area, the better efficiency characteristics of the Type 2D model proved it to be suitable for use with the SMM.

Acknowledgment

This paper is based on results obtained from the Future Pioneering Program “Development of magnetic material technology for high-efficiency motors” commissioned by the New Energy and Industrial Technology Development Organization (NEDO).

References

(1) M. Kamiya: "Development of Traction Drive Motor for the Toyota Hybrid System", IPEC-Niigata 2005, pp.1474–1481 (2005)

(2) K.T. Chau, C.C. Chan, and C. Liu: "Overview of Permanent-Magnet Brushless Drives for Electric and Hybrid Electric Vehicles", *IEEE Trans. Ind. Electron.*, Vol.55, No.6, pp.2246–2257 (2008)

(3) X. Liu, H. Chen, J. Zhao, and A. Belahcen: "Research on the Performances and Parameters of Interior PMSM Used for Electric Vehicles", *IEEE Trans. Ind. Electron.*, Vol.63, No.6, pp.3533–3545 (2016)

(4) J. Nerg, M. Rilla, V. Ruuskanen, J. Pyrhonen, and S. Ruotsalainen: "Direct-Driven Interior Magnet Permanent-Magnet Synchronous Motors for a Full Electric Sports Car", *IEEE Trans. Ind. Electron.*, Vol.61, No.8, pp.4286–4294 (2014)

(5) S. Kim, S. Park, T. Park, J. Cho, W. Kim, and S. Lim: "Investigation and Experimental Verification of a Novel Spoke-Type Ferrite-Magnet Motor for Electric-Vehicle Traction Drive Applications", *IEEE Trans. Ind. Electron.*, Vol.61, No.10, pp.5763–5770 (2014)

(6) J.H. Han, J. Lee, and W.H. Kim: "A Study on Optical Design of the Triangle Type Permanent Magnet in IPMSM Rotor by Using the Box-Behnken Design", *IEEE Trans. Magn.*, Vol.51, No.3, Article 8200704 (2015)

(7) S. Yoshioka, S. Morimoto, M. Sanada, and Y. Inoue: "The Influence of Magnetic Properties of Permanent Magnet on the Performance of IPMSM for Automotive Application", in Proc. IPEC-Hiroshima 2014, pp.246–251 (2014)

(8) Y. Hirayama, Y.K. Takahashi, S. Hirosawa, and K. Hono: "NdFe12Nx Hard-Magnetic Compound with High Magnetization and Anisotropy Field", MATERIALIA, Vol.95, pp.70–72 (2015)

(9) K. Kiyota, T. Kakishima, and A. Chiba: "Comparison of Test Result and Design Stage Prediction of Switched Reluctance Motor Competitive With 60-kW Rare-Earth PM Motor", *IEEE Trans. Ind. Electron.*, Vol.61, No.10, pp.5712–5721 (2014)

(10) S. Yoshioka, S. Morimoto, M. Sanada, and Y. Inoue: "Influence of Magnet Arrangement on the Performance of IPMSMs for Automotive Applications", 2014 IEEE ECCE, pp.4507–4512 (2014)

(11) K. Yamazaki, M. Kumagai, T. Ikemi, and S. Ohki: "A Novel Rotor Design of Interior Permanent-Magnet Synchronous Motors to Cope with Both Maximum Torque and Iron-Loss Reduction", *IEEE Trans. Ind. Appl.,* Vol.49, No.6, pp.2478–2486 (2013)

Yuki Shimizu (Student Member) received the B.E. degree from Osaka Prefecture University, Sakai, Japan, in 2016. He is currently a graduate student in the Department of Electrical and Information Systems, Osaka Prefecture University. His research interests include permanent magnet synchronous machine designs.

Shigeo Morimoto (Senior Member) received the B.E., M.E., and Ph.D. degrees from Osaka Prefecture University, Sakai, Japan, in 1982, 1984, and 1990, respectively. In 1984, he joined Mitsubishi Electric Corporation, Tokyo, Japan. Since 1988, he has been with the Graduate School of Engineering, Osaka Prefecture University, where he is currently a Professor. His main areas of research interest are permanent magnet synchronous machines, reluctance machines and their control systems. Dr. Morimoto is a member of the IEEE, the Society of Instrument and Control Engineers of Japan, the Institute of Systems, Control and Information Engineers, and the Japan Institute of Power Electronics.

Masayuki Sanada (Senior Member) received the B.E., M.E., and Ph.D. degrees from Osaka Prefecture University, Sakai, Japan, in 1989, 1991, and 1994, respectively. Since 1994, he has been with the Graduate School of Engineering, Osaka Prefecture University, where he is currently an Associate Professor. His main areas of research interest are permanent-magnet motors for direct-drive applications, their control systems, and magnetic field analysis. Dr. Sanada is a member of the IEEE, the Japan Institute of Power Electronics, and the Japan Society of Applied Electromagnetics and Mechanics.

Yukinori Inoue (Member) received the B.E., M.E., and Ph.D. degrees from Osaka Prefecture University, Sakai, Japan, in 2005, 2007, and 2010, respectively. Since 2010, he has been with the Graduate School of Engineering, Osaka Prefecture University, where he is currently an Associate Professor. His research interests include control of electrical drives, in particular, the direct torque control of permanent magnet synchronous motors and position sensorless control of these motors. Dr. Inoue is a member of the IEEE and the Japan Institute of Power Electronics.